Cu nanoclusters activating ultrafine Fe₃N nanoparticles via the Mott-Schottky effect for rechargeable zinc-air batteries

Qing Dong [a], Gangjian Li [a], Fangfang Liu [b], Jianwei Ren [c,*], Hui Wang [a], Rongfang Wang [a,*]

[a] *State Key Laboratory Base for Eco-Chemical Engineering, College of Chemical Engineering, Qingdao University of Science and Technology, Qingdao 266042, China*
[b] *Weifang University of Science and Technology, Shouguang, Weifang 262700, China*
[c] *Department of Mechanical Engineering Science, University of Johannesburg, Cnr Kingsway and University Roads, Auckland Park, 2092 Johannesburg, South Africa*

ARTICLE INFO

ABSTRACT

The rational design and synthesis of cost-effective bifunctional oxygen electrocatalysts is crucial for the large-scale commercial applications of rechargeable zinc-air batteries. In this work, the Cu$_{NCs}$/Fe₃N-NPCF catalyst was constructed by anchoring the metallic Cu/Fe₃N ensembles with different sizes onto N-doped porous carbon nanosheets. The Mott-Schottky heterostructure formed by Fe₃N nanoparticles and its surrounding Cu clusters enabled spontaneous electron transfer, which speeded up the electron supply from active sites to various oxygen intermediates. The electrophilic region on Cu side and the nucleophilic region on Fe₃N side improved the adsorption of O₂ and OH⁻, respectively. The Cu$_{NCs}$/Fe₃N-NPCF exhibited onset potential of 0.98 V and low Tafel slope of 59.30 mV dec^{-1} in ORR, and overpotential of 282 mV at 10 mA cm^{-2} current density in OER. The Cu$_{NCs}$/Fe₃N-NPCF-based zinc-air battery displayed the excellent catalytic activity and durability. These findings provided the guides in developing the efficient and stable Mott-Schottky bifunctional oxygen electrocatalysts.

1. Introduction

As one of the efficient energy conversion and storage solutions, metal-air batteries hold the promises to address the increasing energy crisis and environmental pollution problems [1–3]. In literature, the extensive research efforts have been made towards zinc-air batteries (ZABs) because of their advantages such as high specific energy storage capacities [4–6]. However, the experiments found it difficult to fully convert the chemical energy to electricity through the electrocatalytic processes of oxygen reduction reaction (ORR) and oxygen evolution reaction (OER). Instead, the low energy density and low power density were often recorded [7–9]. Specifically, the oxygen electrocatalytic reaction at the cathode involved a complex three-phase process (solid catalyst, liquid electrolyte and gaseous O₂), in which reactants, oxygen-containing intermediates (i.e., OH⁻, O⁻ and OOH⁻), the multiple adsorption/desorption steps and complex multi-electron transfer processes of the products resulted in slow ORR and OER reaction kinetics [10,11]. Although the RuO₂/IrO₂-based catalysts are still widely used in ORR and OER processes [12,13], their high costs limited the large-scale application and development of rechargeable ZABs [14,15]. Therefore, it is imperative to design and develop cost-effective electrocatalysts with bifunctional catalytic activity and good durability [16,17].

In this regard, the transition metal-nitrogen-carbon (M-N$_x$-C) catalysts found a wide application in ORR due to its unique electron configuration [18–20]. Especially, the cost-effective iron and nitrogen co-doped carbon (Fe-N$_x$-C) catalysts have been considered as one of the most promising candidates due to their Pt-like catalytic activities [21–23]. The introduction of iron nitride (Fe₂N and Fe₃N) particles with rich active sites into the carbon matrix has been demonstrated as an efficient route for the preparation of Fe-N$_x$-C catalysts [24–26]. For instance, Mu et al. [8] indirectly embedded Fe₃N particles into 3D zeolitic-imidazole frameworks (ZIF) structures to prepare ORR catalysts of ZFN-900 with enhanced performance for ZABs. In the experiments of Zhou at al. [27], the P-Fe₃N @ NC NSs/IF composite catalyst was prepared by wrapping phosphorus-hybridized iron nitride nanoparticles with nitrogen-hybrid carbon nanosheets on Fe foam substrates. Further, the N and P anions were doped to enhance the OER electrocatalytic activity of Fe₃N active center. Alternatively, some researchers tackled the intrinsic activity of the Fe₃N phase through interfacial engineering strategies. As demonstrated, Qiu et al. [28] constructed Ni₃N/Fe₃N heterostructure with rich active interface sites by grafting Fe₃N nanoparticles onto Ni₃N nanosheets to improve OER electrocatalytic activity of Ni₃N @ Fe₃N/CF-6 catalyst. Ma and co-workers [29] prepared a highly efficient Fe-V-based heterogeneous electrocatalyst by fabricating

active metal nitrides (FeN, Fe$_3$N and VN) on the Fe-V oxide surface and the enhanced OER electrocatalytic activity of N-FVO catalyst was derived. With those efforts, it was found that the intrinsic activity of the catalysts was difficult to improve, as the uncontrollable high-temperature pyrolysis process and harsh gas reaction conditions often led to the agglomeration of iron nitride nanoparticles. In addition, although the catalytic activity of iron nitride can be optimized through interface regulation, the relatively poor electrical conductivity often caused an excessively high overpotential for the catalytic reaction. Therefore, it remains as a crucial challenge to realize the bifunctional oxygen electrocatalytic activity of iron nitrides in practical ZABs devices [8,26,30].

From the literature point of view, the heterostructures can be created by compositing the metal ensembles with different sizes and Fe$_3$N phases. With this, the prerequisite for bifunctional oxygen electro-catalysts can be met sufficiently such as rich active sites, the adsorbed oxygen-containing intermediates, and the improved intrinsic activities [16,31–33]. As pointed out by Choi et al. [34], the oxygen reduction catalytic activity of Pt clusters and Pt nanoparticles was superior to that of Pt atom when comparing three Pt/C catalysts with different Pt particle sizes. Besides, metal clusters can couple with ultra-small metal nanoparticles into a better metal ensemble [35,36]. Based on the Mott-Schottky effect, metal hetero-ensembles can be constructed by utilizing the differentiated Fermi level of different metals. This allows to modulate the electron cloud density of the metal ensembles at the atomic level and optimize the reaction activation energy. Meanwhile, the built-in electric field in Mott-Schottky heterostructures can also be tuned through adjusting the density of metal ensembles to accelerate electron transport, so as that the catalytic reactivity of the composite catalyst can be enhanced ultimately [6,32,33]. Moreover, the nitrogen-containing carbon structure with hierarchical pores can be constructed by molten salt-assisted pyrolysis strategy to confine metal nanoparticles. As a result, the ORR and OER were improved through enhancing metal-support interactions, optimizing mass transport capacity, and increasing reaction area as promoter of catalytic activity [24,37]. In view of the above analysis, it is promising to construct a composite catalyst containing both Mott-Schottky heterometallic ensembles of different sizes and nitrogen-doped carbon nanosheets with rich hierarchical pores as efficient bifunctional oxygen electrocatalysts for ZABs.

In this work, the three-dimensional (3D) porous carbon nanosheet frameworks (PCF) was used as substrate to couple highly conductive Cu clusters with ultrafine Fe$_3$N nanoparticles. A Mott-Schottky hetero-metallic ensemble composite catalyst (Cu$_{NCs}$/Fe$_3$N-NPCF) with different sizes was constructed as the air cathode for rechargeable ZABs. The experiments showed that the Fe$_3$N nanoparticles with sizes around 4.5 nm together with Cu clusters were uniformly dispersed within the composite structure. Meanwhile, the spontaneous electron transfer was evidenced at the Cu$_{NCs}$/Fe$_3$N interface between the electrophilic region on the Cu side and the nucleophilic region on the Fe$_3$N side. In addition, the Mott-Schottky nanoreactors with built-in circuits has highly dispersed metal ensembles, large accessible surface area and open hierarchical pore structure, which can provide more active sites, fast electrolytes diffusion pathways and highly open mass transport pathways to greatly enhance the oxygen electrocatalytic activity. The performance evaluation of the optimal Cu$_{NCs}$/Fe$_3$N-NPCF catalyst in alkaline medium showed that the potential difference $\triangle E$ of the catalyst was only 0.66 V. The Cu$_{NCs}$/Fe$_3$N-NPCF-assembled rechargeable ZAB delivered an open-circuit voltage of 1.48 V and a power density of 133.20 mW cm^{-2} at a current density of 235 mA cm^{-2}. This work presented a feasible strategy to construct Mott-Schottky electrocatalysts with fast electron transfer and mass transport in developing the practical ZABs.

2. Experimental

2.1. Materials

Copper chloride dihydrate (CuCl$_2$·2H$_2$O, ≥99%), ferric chloride hexahydrate (FeCl$_3$·6H$_2$O, ≥99%), polyvinyl pyrrolidone ((C$_6$H$_9$NO)$_n$, k30), urea (CH$_4$N$_2$O , ≥99%), peptone (total nitrogen≥14.5%, amino nitrogen≥2.5%), sodium Chloride (NaCl, ≥99%) and nitric acid (HNO$_3$, 68%) were purchased from Sinopharm Chemical Reagent Co., Ltd. All reagents are analytically pure and used directly without further purifications.

2.2. Preparation of porous carbon nanosheet framework (PCF) substrate

The 3D porous carbon nanosheet framework (PCF) substrate was prepared by a molten salt-assisted pyrolysis approach, as shown in Fig. S1. In the experiments, 1 g of peptone and 10 g of NaCl were mixed in a ball mill for 6 h at 550 rpm. The ball-milled mixture was transferred to a porcelain boat in a tube furnace. After purging by N$_2$ flow (99.9% purity) for 10 min, the furnace was heated to 900 °C at a heating rate of 5 °C min^{-1} in the flowing N$_2$ atmosphere and kept at that temperature for 2 h. The furnace was then cooled down to 30 °C at a cooling rate of 5 °C min^{-1}. The obtained product was rinsed with deionized water by suction filtration to remove surface impurities. The product was dried in a blast dryer at 60 °C for 6 h to obtain a preliminary sample. Afterwards, 1 g of the preliminary sample was refluxed in 2 M HNO$_3$ solution at 80 °C for 12 h. Lastly, the product was rinsed to neutral with deionized water and dried in an oven at 60 °C for 6 h to obtain a 3D PCF sample.

2.3. The preparation of Cu$_{NCs}$/Fe$_3$N-NPCF sample

Firstly, 50 mg of PCF sample, 0.06 mmol of FeCl$_3$·6H$_2$O, 0.06 mmol of CuCl$_2$·2H$_2$O and 29.54 mg PVP were placed together in a 100 mL polytetrafluoroethylene reactor. After adding 30 mL of deionized water, the mixture was stirred at room temperature for 30 min. Then, the hydrothermal reaction was carried out in a blast drying oven at 160 °C for 12 h. The product was centrifuged out and dried to obtain the Cu/Fe$_2$O$_3$-NPCF precursor. Secondly, 30 mg of Cu/Fe$_2$O$_3$-NPCF precursor sample and 3.0 g of urea were placed at downstream and upstream position of a tube furnace, respectively. After purging with N$_2$ for 10 min, the furnace was heated up to 600 °C at a heating rate of 5 °C min^{-1} and held at that temperature for 2 h. After cooling down to 30 °C at a cooling rate of 5 °C min^{-1}, the Cu$_{NCs}$/Fe$_3$N-NPCF sample was obtained. For comparison, under the same experimental conditions, the Fe$_3$N-NPCF sample was also prepared by using 50 mg of PCF, 0.06 mmol of FeCl$_3$·6H$_2$O and 29.54 mg of PVP. Similarly, the Cu$_{NCs}$-NPCF sample was prepared by using 50 mg of PCF, 0.06 mmol of CuCl$_2$·2 H$_2$O and 29.54 mg of PVP. Lastly, the NPCF sample was prepared with 50 mg of PCF and 29.54 mg of PVP.

2.4. Performance evaluation on the as-prepared samples

The information of the textural characterization and electrochemical tests on the as-prepared samples can be referred to the Supporting Information.

3. Result and discussion

3.1. Catalyst synthesis and characterization

The preparation process of the Cu$_{NCs}$/Fe$_3$N-NPCF sample is illustrated in Fig. 1a. Based on the molecular design from the previous work [24,37], the 3D PCF was chosen as the anchoring carbon platform (ACP). The containing abundant edge sites and a small amount of nitrogen dopants appeared effective in alleviating the agglomeration of metallic species during wet deposition while forming a highly
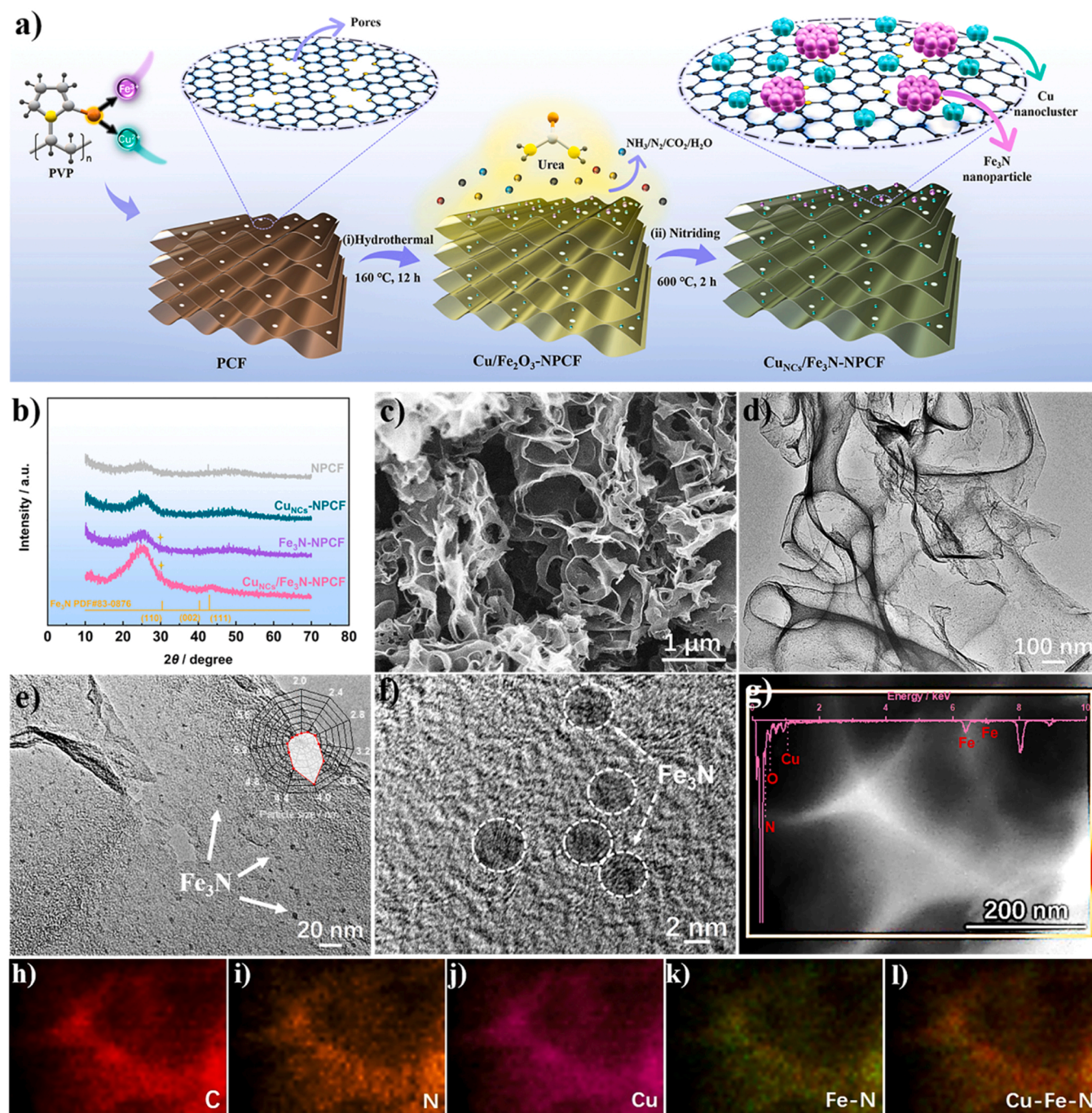
Fig. 1. (a) Schematic illustration for the synthesis of the Cu_{NCs}/Fe_3N-NPCF sample. (b) XRD patterns of NPCF, Cu_{NCs}-NPCF, Fe_3N-NPCF and Cu_{NCs}/Fe_3N-NPCF samples. (c) SEM image, (d—f) TEM images and (g) STEM image of Cu_{NCs}/Fe_3N-NPCF sample. Elemental mapping images of (h) C, (i) N, (j) Cu, (k) Fe-N and (l) Cu-Fe-N elements.

graphitized carbon framework (Fig. S2). After the further N-doping process, the textural properties of the NPCF substrate remained well, and its near-surface doped-N content increased to 4.8% (Fig. S3). In the process of wet deposition, polyvinylpyrrolidone (PVP) played a dual key role: (i) To firmly anchor Cu^{2+}/Fe^{3+} ions through the donation of lone pair electrons in C=O and form metal-oxygen coordination bonds. (ii) To create a porous structure during the pyrolysis process with high N-doping content. The XRD pattern of the Cu/Fe_2O_3-NPCF sample in Fig. S4 shows that Fe_2O_3 particles are formed through Fe-O coordination bonds during the hydrothermal reaction. The SEM and TEM images of Cu/Fe_2O_3-NPCF sample in Fig. S5 show that the structure of PCF substrate is well preserved after loading of metal particles. The energy

dispersive X-ray (EDX) elemental mapping images confirm the presence of Cu and Fe species in the Cu/Fe_2O_3-PNCF composite structure. Sequentially, the obtained Cu/Fe_2O_3-NPCF sample was annealed at 600 °C in an ammonia gas atmosphere provided by urea, which aimed to remove residual ligands, enhance the interaction between the metal and the substrate, and further increase the N-doping content. At this temperature of 600 °C, Fe_2O_3 particles were converted into Fe_3N nanoparticles via ion exchange reaction with ammonia gas. Eventually, the Cu_{NCs}/Fe_3N-NPCF composite consisting of Cu clusters and ultrafine Fe_3N nanoparticles was prepared. As observed from the XRD pattern of the prepared Cu_{NCs}/Fe_3N-NPCF sample in Fig. 1b, the diffraction peaks at 25.2° and 43.6° correspond to the (002) and (101) planes of amorphous

carbon, respectively [24], while the diffraction peak at 30.3° is assigned to the (110) crystal plane of Fe$_3$N (PDF#83–0876) [38]. Compared with those of the NPCF, CuNCs-NPCF and Fe$_3$N-NPCF samples, the (002) characteristic diffraction peak of Cu$_{NCs}$/Fe$_3$N-NPCF sample is relatively sharper, and this implies that the coupled Cu/Fe$_3$N two phases improved the degree of graphitization of the carbon composite. The SEM image (Fig. 1c) and TEM image (Fig. 1d) show the intact structure of Cu$_{NCs}$/-Fe$_3$N-NPCF sample after high-temperature nitridation treatment and no obvious metal particles are visible. After the further magnification, ultrafine Fe$_3$N nanoparticles with sizes around 4.0 nm (highlighted by white arrows) appeared on the surface of the porous carbon nanosheets (Fig. 1e). It is worth noting that those Fe$_3$N nanoparticles (highlighted by white dashed circles) are surrounded by Cu clusters, as evidenced by the high-magnification transmission electron microscope (TEM) image in Fig. 1f. The TEM images of Cu$_{NCs}$-NPCF sample in Fig. S6 further confirm the presence of the Cu clusters on the porous carbon nanosheets. The scanning transmission electron microscopy (STEM) images of Cu$_{NCs}$/Fe$_3$N-NPCF sample in Fig. 1g and the EDX elemental mapping in Fig. 1h-j illustrate the well-dispersed N and Cu elements within the composite structure. Besides, the elemental mapping images of Cu and Fe-N in Fig. 1l suggest the overlapping of Cu and Fe$_3$N two phases. Those observations inform that the heterogeneous metal ensembles containing Cu clusters and ultrafine Fe$_3$N nanoparticles with different sizes have been successfully anchored on the NPCF substrate. By varying the ratios of Cu and Fe atoms (n_{Cu}:n_{Fe}) in the metal precursors, the Cu$_{NCs}$/-Fe$_3$N$_{(0.5:1)}$-NPCF, Cu$_{NCs}$/Fe$_3$N$_{(1:1)}$-NPCF and Cu$_{NCs}$/Fe$_3$N$_{(1.5:1)}$-NPCF samples were prepared with different density and different sizes of metal ensembles. As indicated by the TEM images of Cu$_{NCs}$/Fe$_3$N$_{(0.5:1)}$-NPCF, Cu$_{NCs}$/Fe$_3$N$_{(1:1)}$-NPCF and Cu$_{NCs}$/Fe$_3$N$_{(1.5:1)}$-NPCF samples in Fig. 2 and Fig. S7, a small amount of Cu atoms hardly affects the sizes of Fe$_3$N nanoparticles (Fig. 2a). With the increasing ratio of n_{Cu}:n_{Fe}, Cu clusters are enriched around Fe$_3$N particles (Fig. 2b). However, the gradual agglomeration of Cu clusters and Fe$_3$N nanoparticles will decrease the effective contact density of the metal ensembles (Fig. 2c) [39].

Fig. 3a shows the Raman spectra of NPCF and Cu$_{NCs}$/Fe$_3$N-NPCF two samples, in which the peaks around 1350 cm^{-1} and 1580 cm^{-1} correspond to the D and G bands. Usually, the intensity ratios of I_D/I_G are used to describe the level of surface defects or the degree of graphitization of a given material [40]. More specifically, the smaller I_D/I_G value of 0.93 from the Cu$_{NCs}$/Fe$_3$N-NPCF sample than that of NPCF sample (I_D/I_G=0.97) indicates that the coupled Cu/Fe$_3$N phases enhanced the

degree of graphitization of the porous carbon nanosheets. In comparison with NPCF sample, the Raman bands of Cu$_{NCs}$/Fe$_3$N-NPCF sample exhibits an obvious blue-shift phenomenon, which attributes to the Mott-Schottky effect with more electrons passing through the metal-nitrogen-carbon heterogeneity. Thus, the transition of mass interface from the metallic Cu/Fe$_3$N phase to the surface of the nitrogen-doped carbon layer caused the shifts of the D and G bands of the carbon structure [41]. Further, Fig. 3b displays the N$_2$ adsorption-desorption isotherms of the as-prepared samples. As seen, four samples of NPCF, Cu$_{NCs}$-NPCF, Fe$_3$N-NPCF and Cu$_{NCs}$/Fe$_3$N-NPCF exhibit the similar type *IV* isotherms [24]. In contrast, the dramatically increasing adsorption at the low-pressure region suggests the existence of large amount of micropores (0.5–2.0 nm) within the Cu$_{NCs}$/-Fe$_3$N-NPCF sample, which is supported by the pore-size-distribution curves in Fig. 3d. Meanwhile, the weak hysteresis loop at high-pressure region suggests the coexistence of mesopores (2.0–6.0 nm) [24]. With specific interests, Fig. 3c illustrates the changes in total surface area, micropore surface area, and external surface area from the four samples. Clearly, the metal-loading on the NPCF substrate decreased the surface area of the catalyst sample. The well-dispersed ultrafine Fe$_3$N nanoparticles within the Cu$_{NCs}$/Fe$_3$N-NPCF composite sample result in a larger specific surface area (437.6 m^2 g^{-1}) in comparison with that of the Fe$_3$N-NPCF sample (310.2 m^2 g^{-1}). Table S1 lists the structural advantage of the prepared Cu$_{NCs}$/Fe$_3$N-NPCF composite catalyst over other catalysts reported in literature. As predicted, the micropores will expose more active sites on the sample surface while the mesopores will effectively increase the contact of the catalyst surface with the electrolyte. This is beneficial to the adsorption of reactants and the dissociation of intermediates from the Cu$_{NCs}$/Fe$_3$N-NPCF sample surface [9].

3.2. Electrochemical performance

The ORR catalytic activity of the as-prepared Cu$_{NCs}$/Fe$_3$N-NPCF sample was evaluated using a three-electrode setup in 0.1 M KOH electrolyte. Compared to the cyclic voltammetry (CV) curve under N$_2$, the CV curve of the Cu$_{NCs}$/Fe$_3$N-NPCF sample under O$_2$ saturated condition displays an obvious catalytic oxygen reduction activity with a characteristic oxygen reduction peak (Fig. S8). To further illustrate the advantages of Cu$_{NCs}$/Fe$_3$N-NPCF catalyst, Fig. 4a-b compares the ORR performance of Cu$_{NCs}$/Fe$_3$N-NPCF, NPCF, Cu$_{NCs}$-NPCF, Fe$_3$N-NPCF and
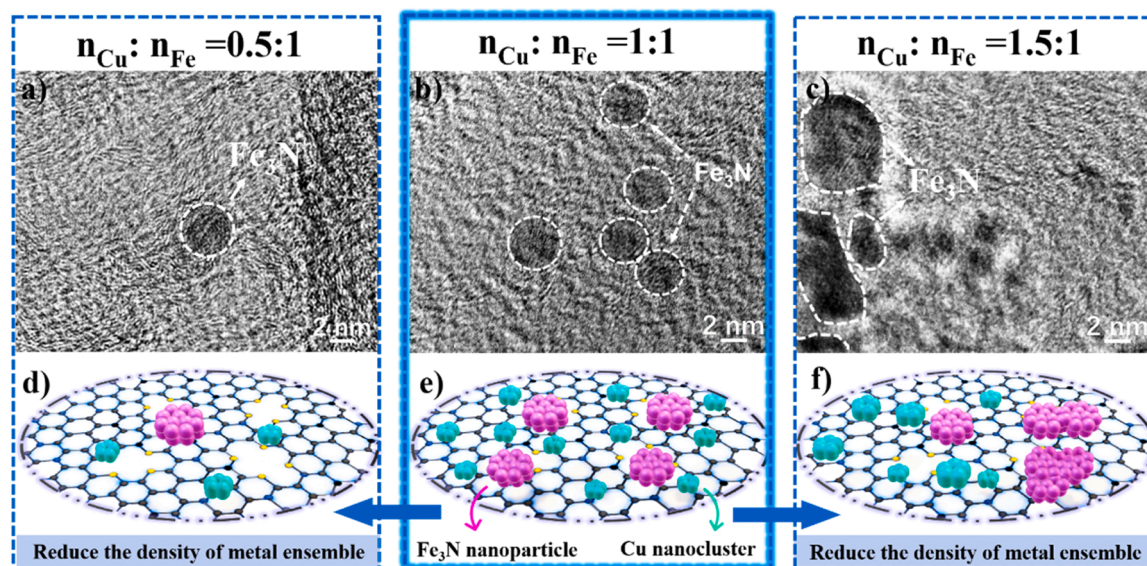
Fig. 2. TEM images of (a) Cu$_{NCs}$/Fe$_3$N$_{(0.5:1)}$-NPCF sample, (b) Cu$_{NCs}$/Fe$_3$N$_{(1:1)}$-NPCF sample, and (c) Cu$_{NCs}$/Fe$_3$N$_{(1.5:1)}$-NPCF sample. (d—f) Schematic diagrams of the structural evolution from Cu$_{NCs}$/Fe$_3$N$_{(0.5:1)}$-NPCF and Cu$_{NCs}$/Fe$_3$N$_{(1:1)}$-NPCF to Cu$_{NCs}$/Fe$_3$N$_{(1.5:1)}$-NPCF samples.
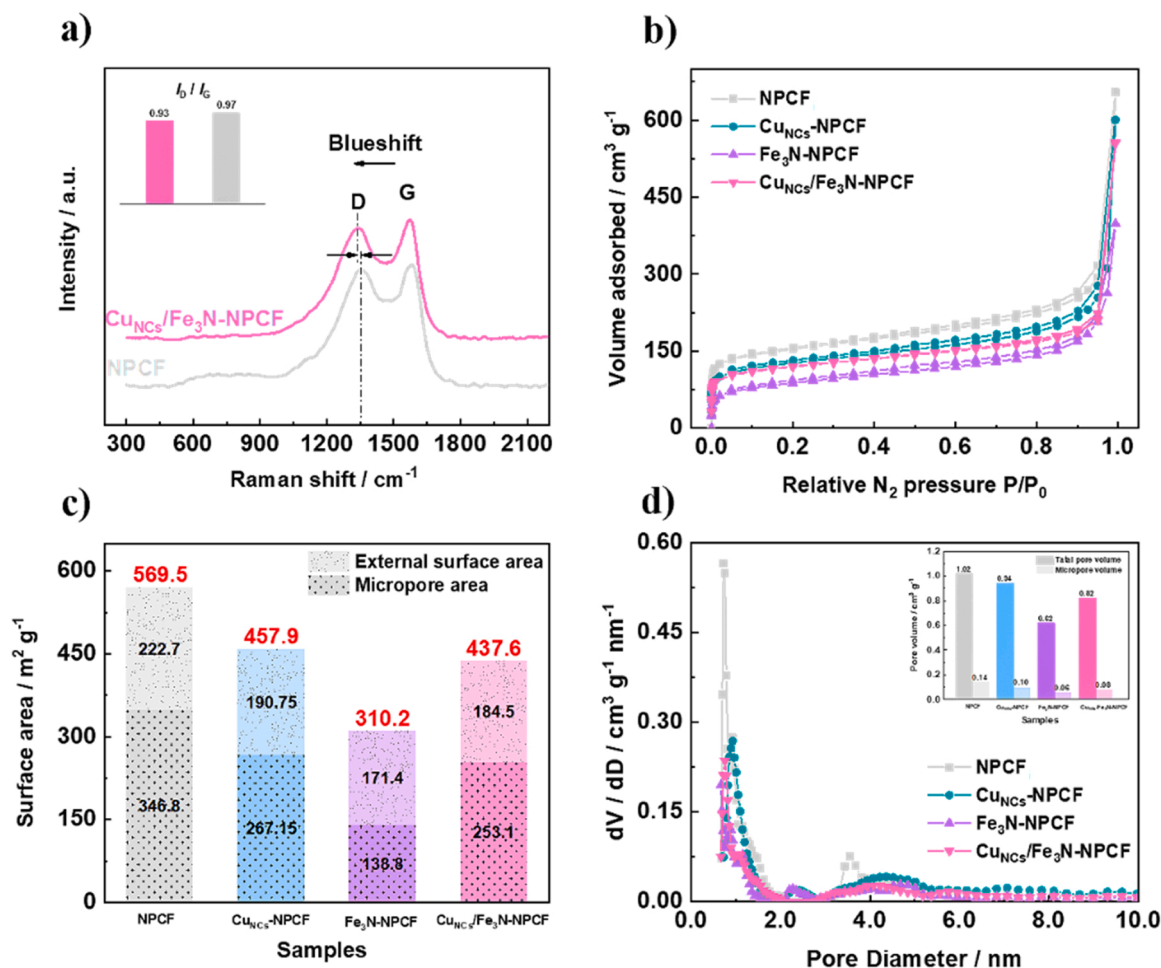
Fig. 3. (a) Raman spectra and $\frac{I_D}{I_G}$ values of NPCF and Cu_{NCs}/Fe_3N-NPCF samples. (b) N_2 adsorption-desorption isotherms, (c) Surface area, external surface area and micropore area, (d) Pore-size-distributions curves and pore volumes of NPCF, Cu_{NCs}-NPCF, Fe_3N-NPCF and Cu_{NCs}/Fe_3N-NPCF samples.

commercial 20% Pt/C catalyst five samples. As seen, the potential (E_{onset}) and half-wave potential ($E_{1/2}$) of the Cu_{NCs}/Fe_3N-NPCF sample are 0.98 V and 0.85 V, respectively, which are slightly better than those of the commercial 20% Pt/C sample ($E_{onset} = 0.97$ V, $E_{1/2} = 0.84$ V). Referred to the single-metal Fe_3N-NPCF sample, the Cu_{NCs}/Fe_3N-NPCF sample exhibits a higher onset potential, half-wave potential and limiting current density of J_L (6.01 mA cm^{-2}). This implies that the Mott-Schottky heterostructure created by the addition of metallic Cu enhanced the ORR catalytic activity. As illustrated in Fig. S9, at a constant temperature of 30 °C, the Cu_{NCs}/Fe_3N-NPCF sample displays a higher specific activity (i.e. kinetic current per unit surface area of catalyst) as well as a better intrinsic catalytic activity than those of the Fe_3N-NPCF and Cu_{NCs}-NPCF catalyst samples. Meanwhile, the smaller Tafel slope of Cu_{NCs}/Fe_3N-NPCF sample (59.30 mV dec^{-1}) than that of Cu_{NCs}-NPCF (62.10 mV dec^{-1}) and Fe_3N-NPCF (68.70 mV dec^{-1}) catalyst samples suggests that Mott-Schottky heterostructure composed of Cu clusters and Fe_3N nanoparticles significantly improved the ORR kinetics [32] (Fig. 4c). The differentiated Nyquist plots of Cu_{NCs}-/Fe_3N-NPCF, NPCF, Cu_{NCs}-NPCF, and Fe_3N-NPCF four samples in Fig. S10 further suggests that the Cu_{NCs}/Fe_3N-NPCF catalyst sample has a faster charge transfer process. To explore the specific contribution of Cu clusters to ORR performance in Cu_{NCs}/Fe_3N-NPCF heterostructures, the catalyst samples with different ratios of Cu/Fe atoms are tested under the same conditions. Fig. S11a shows the ORR linear voltammetry curves of $Cu_{NCs}/Fe_3N_{(0.5:1)}$-NPCF, $Cu_{NCs}/Fe_3N_{(1:1)}$-NPCF and Cu_{NCs}-/$Fe_3N_{(1.5:1)}$-NPCF samples. By taking into consideration of the E_{onset}, $E_{1/2}$ and $J_{E=0.5\ V\ vs.\ RHE}$ values of each catalyst in Fig. S11b, Tafel slope values

in Fig. S11c and electron transfer numbers in Fig. S11d, it allows us to conclude that the higher densities of Cu/Fe_3N metal ensembles within the $Cu_{NCs}/Fe_3N_{(1:1)}$-NPCF catalyst structure improved the ORR electrocatalytic activity more effectively. Besides, several intermediate samples were prepared by varying the nitridation temperature to understand the contribution of Fe_3N metal in the ORR process. As observed in Fig. S12, with the increasing nitridation temperatures, the Fe_2O_3 phase within the Cu/Fe_2O_3-NPCF samples transforms gradually into the Fe_3N phase, and the oxygen reduction catalytic performance increases along with the increasing nitridation temperatures (Fig. S13). These results indicate that Fe_3N nanoparticles are the main active component within the Cu_{NCs}/Fe_3N-NPCF heterocatalyst for the oxygen reduction electrocatalytic reaction. The comparison of ORR electrocatalytic performance in Table S2 shows that the prepared Cu_{NCs}/Fe_3N-NPCF Mott-Schottky heterocatalyst outperformed other carbon-based ORR electrocatalysts reported in literature. In addition, the LSV curves of Cu_{NCs}/Fe_3N-NPCF, commercial 20% Pt/C, NPCF, Cu_{NCs}-NPCF and Fe_3N-NPCF catalyst samples are recorded on rotating disk electrodes at different rotational speeds under oxygen saturation. The results in Fig. 4d and Fig. S14 illustrates that the limiting current density on the LSV curves of Cu_{NCs}-/Fe_3N-NPCF sample increases with the rotating disk speed. This implies that the ORR process is limited by the oxygen concentration of the reactants. To further evaluate their ORR catalytic efficiencies, the H_2O_2 yields and electron transfer numbers during the ORR from 20% Pt/C, NPCF, Cu_{NCs}-NPCF, Fe_3N-NPCF and Cu_{NCs}/Fe_3N-NPCF catalyst samples were calculated by the rotating ring-disk technique (RRDE). As shown in Fig. 4e and Fig. S15b, at the potential of 0.5 V vs. RHE, the H_2O_2 yield of
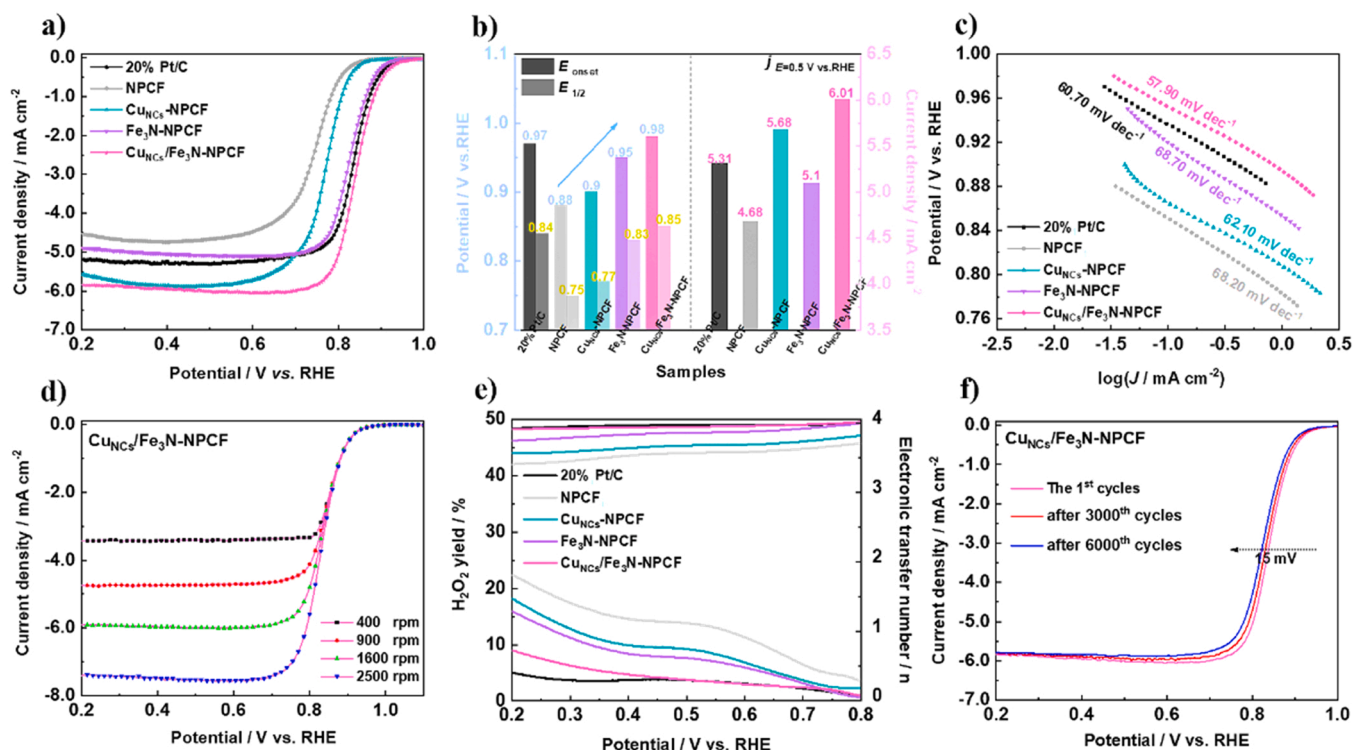
Fig. 4. (a) ORR linear scan voltammograms (LSV) curves of the as-prepared samples at 1600 rpm in an O_2-saturated 0.10 M KOH with a scan rate of 5 mV s^{-1}, (b) Corresponding E_{onset}, $E_{1/2}$ and $J_{E=0.5\,V\,vs.\,RHE}$, and (c) Tafel plots of 20% Pt/C, NPCF, Cu$_{NCs}$-NPCF, Fe$_3$N-NPCF and Cu$_{NCs}$/Fe$_3$N-NPCF samples. (d) LSV curves of Cu$_{NCs}$/Fe$_3$N-NPCF sample on RDE in O_2-saturated 0.1 M KOH solution at various rotation rates, (e) H$_2$O$_2$ yield and electron transfer number plots of 20% Pt/C, NPCF, Cu$_{NCs}$-NPCF, Fe$_3$N-NPCF and Cu$_{NCs}$/Fe$_3$N-NPCF samples. (f) LSV curves of the 1st, 3000th cycles and 6000th cycles for ORR on Cu$_{NCs}$/Fe$_3$N-NPCF electrode sample in an O_2-saturated 0.10 M KOH with a scan rate of 5 mV s^{-1}.

Fe$_3$N-NPCF catalyst sample is about 7.65%, and the electron transfer number is only 3.86. However, the H$_2$O$_2$ yield of the Cu$_{NCs}$/Fe$_3$N-NPCF heterocatalyst decreases to 3.77% and its electron transfer number reached 3.94 during the oxygen reduction process. Such an ORR catalytic efficiency appears comparable to that of the commercial 20% Pt/C catalyst at the same potential of 0.5 V with a H$_2$O$_2$ yield of 3.68% and an electron transfer number of 3.98. Those results suggest that the Cu clusters and ultrafine Fe$_3$N nanoparticles within the Cu$_{NCs}$/Fe$_3$N-NPCF heterocatalyst accelerated the transfer of various oxygen-containing intermediates during the ORR with a high four-electron selectivity [42]. Lastly, the stability of the Cu$_{NCs}$/Fe$_3$N-NPCF catalyst sample in the ORR process was evaluated. In contrast, the LSV curve of the Cu$_{NCs}$/-Fe$_3$N-NPCF catalyst in O$_2$-saturated 0.1 M KOH electrolyte solution shifts to the left by 15 mV and the limiting current density decreases by only 1.9% after 6000 cycles (Fig. 4f). However, the half-wave potential and the limiting current density of the commercial 20% Pt/C catalyst sample decrease by 48 mV and 2.5%, respectively, under the same testing conditions (Fig. S16). At this point, the prepared Cu$_{NCs}$/-Fe$_3$N-NPCF catalyst sample exhibited a better stability than the commercial 20% Pt/C catalyst.

Subsequently, Fig. 5a-b show the OER activities of the NPCF, Cu$_{NCs}$-NPCF, Fe$_3$N-NPCF and Cu$_{NCs}$/Fe$_3$N-NPCF catalyst samples in 1 M KOH electrolyte comparing with the commercial RuO$_2$ sample. As seen, the overpotential of Cu$_{NCs}$/Fe$_3$N-NPCF catalyst sample at a current density of 10 mA cm^{-2} is only 282 mV, which is better than that of Cu$_{NCs}$-NPCF (330 mV), Fe$_3$N-NPCF (317 mV) and commercial RuO$_2$ (287 mV) samples. This reflects the positive role of the Mott-Schottky heterostructure within the Cu$_{NCs}$/Fe$_3$N-NPCF catalyst in enhancing the OER catalytic performance. The OER kinetic performance of the catalysts are further investigated by the Tafel curves in Fig. 5c [43]. As the Tafel slope represents the growth rate of the current to the overpotential, a smaller Tafel slope means a faster increase of the current density of the catalyst.

Meanwhile, a smaller overpotential change and a faster reaction rate constant implies a better catalytic activity of the catalyst. Apparently, the Tafel slope of Cu$_{NCs}$/Fe$_3$N-NPCF sample (60.70 mV dec^{-1}) is much smaller than that of Cu$_{NCs}$-NPCF (115.20 mV dec^{-1}), Fe$_3$N-NPCF (100.40 mV dec^{-1}) and RuO$_2$ (85.20 mV dec^{-1}) samples. This endows the Cu$_{NCs}$/Fe$_3$N-NPCF catalyst sample with advantages in the OER reaction, and the rate-determining step of this catalyst is at the end of the multiple electron transfer reaction. Similarly, the prepared Cu$_{NCs}$/-Fe$_3$N-NPCF catalyst sample shows a clear OER catalytic advantage over other reported non-PGM electrocatalysts in comparing the overpotential $E_{j=10\,mA\,cm^{-2}}$ and Tafel slop values (Table S3). Followed, the electrochemical impedance spectroscopy (EIS) was employed to study the interfacial charge transfer behavior of the prepared catalysts. The Cu$_{NCs}$/Fe$_3$N-NPCF catalyst sample shows the smaller semicircle diameter in Fig. 5d at the low frequency region, which suggests that the charge transfer resistance (R_{ct}) of Cu$_{NCs}$/Fe$_3$N-NPCF sample is lower than that of Cu$_{NCs}$-NPCF and Fe$_3$N-NPCF samples (Table S4). In other words, the introduction of Cu/Fe$_3$N metal ensembles with different sizes into NPCF has effectively enhanced the charge transfer rate after modulating the electronic structure in the Mott-Schottky heterostructure [44]. Under the same testing conditions, the OER catalyst activities of Cu$_{NCs}$/Fe$_3$N$_{(0.5:1)}$-NPCF, Cu$_{NCs}$/Fe$_3$N$_{(1:1)}$-NPCF, and Cu$_{NCs}$/Fe$_3$N$_{(1.5:1)}$-NPCF samples are recorded in Fig. S17. For comparison, the OER catalyst activities of Cu$_{NCs}$/Fe$_3$N$_{(0.5:1)}$-NPCF, Cu$_{NCs}$/-Fe$_3$N$_{(1:1)}$-NPCF, and Cu$_{NCs}$/Fe$_3$N$_{(1.5:1)}$-NPCF samples derived at nitridation temperatures of 500 °C, 550 °C, and 600 °C are also shown in Fig. S18. Similar to the ORR testing results, the Cu$_{NCs}$/Fe$_3$N-NPCF catalyst sample prepared at n$_{Cu}$:n$_{Fe}$= 1:1 with nitridation temperature of 600 °C also exhibited the best OER activity compared to other samples. In addition, the individual electrochemically active surface area (ECSA) value is evaluated in Fig. S19 by measuring the electrochemical double-layer capacitance (C$_{dl}$) of each catalyst in the Faradaic region. As
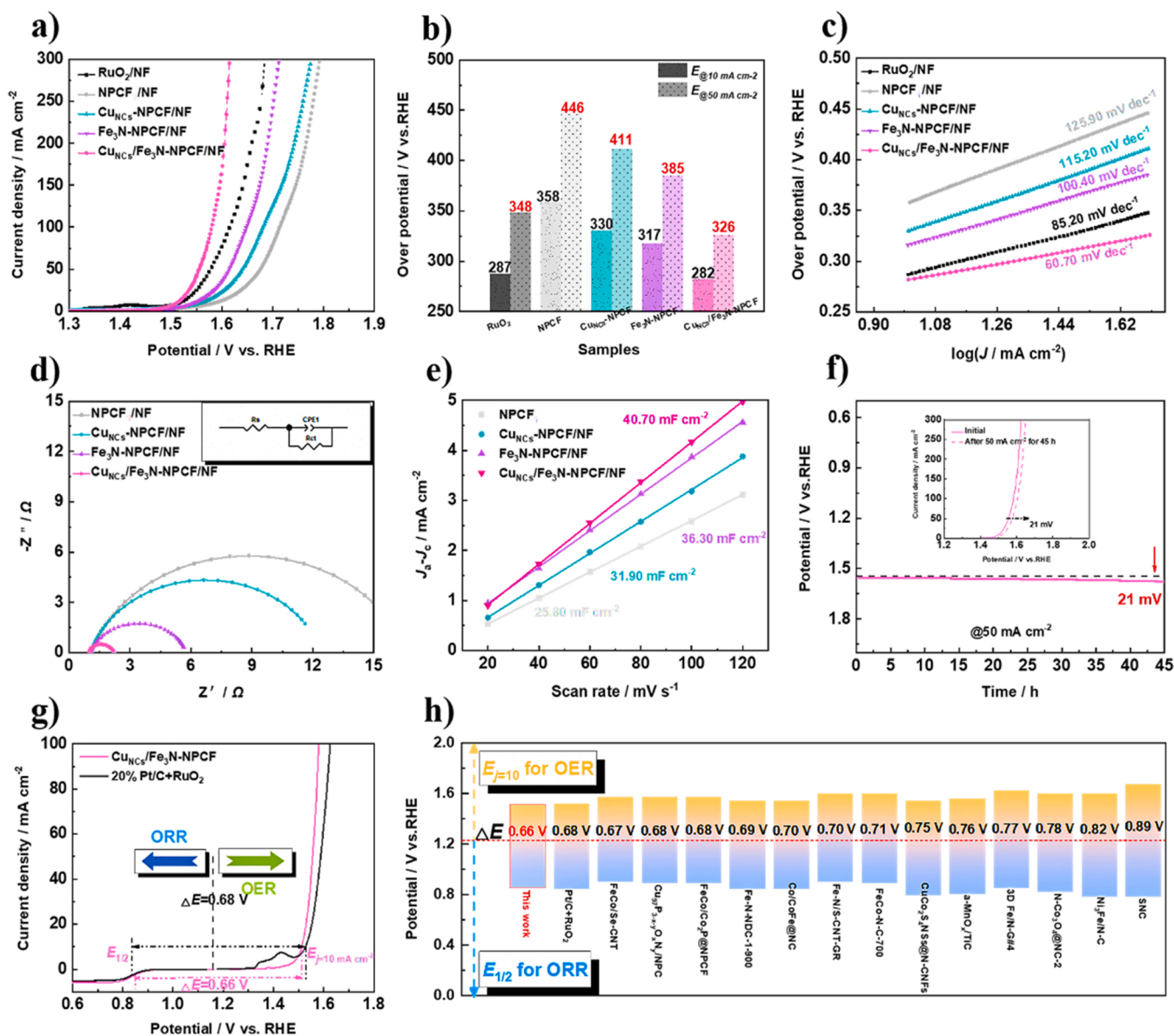
Fig. 5. (a) OER LSV curves in 1.0 M KOH with a scan rate of 5 mV s^{-1}, (b) OER overpotentials at 10 and 50 mA cm^{-2} and (c) Corresponding Tafel plots of RuO$_2$/NF, NPCF/NF, Cu$_{NCs}$-NPCF/NF, Fe$_3$N-NPCF/NF and Cu$_{NCs}$/Fe$_3$N-NPCF/NF samples. (d) Nyquist plots at + 1.56 V vs. RHE, (e) Plots of the current density at 0.566 V versus the scan rate of NPCF/NF, Cu$_{NCs}$-NPCF/NF, Fe$_3$N-NPCF/NF and Cu$_{NCs}$/Fe$_3$N-NPCF/NF samples. (f) Chronoamperometry of Cu$_{NCs}$/Fe$_3$N-NPCF/NF sample at 50 mA cm^{-2} for 45 h (inset: OER LSV curves of the Cu$_{NCs}$/Fe$_3$N-NPCF/NF electrode sample before and after 24 h at 50 mA cm^{-2} in 1.0 M KOH at a scan rate of 5 mV s^{-1}). (g) The entire LSV curves for bifunctional activities within the ORR and OER potential window of 20% Pt/C+RuO$_2$ and Cu$_{NCs}$/Fe$_3$N-NPCF/NF samples. (h) Comparing diagram of the ΔE values of Cu$_{NCs}$/Fe$_3$N-NPCF sample with other reported non-PGM electrocatalysts (also see Table S6 in Supplemental Information).

illustrated in Fig. 5e, C$_{dl}$ value of Cu$_{NCs}$/Fe$_3$N-NPCF sample (40.70 mF cm^{-2}) is larger than that of Cu$_{NCs}$-NPCF (31.90 mF cm^{-2}) and Fe$_3$N-NPCF (36.30 mF cm^{-2}) samples. Again, the larger ECSA value of the Cu$_{NCs}$/Fe$_3$N-NPCF sample attributes to the structural defects with more exposed active sites at the heterointerface in the OER process, which are created by the different lattice spacing between Cu, Fe$_3$N and NPCF phases [45]. The chronoamperometry of Cu$_{NCs}$/Fe$_3$N-NPCF catalyst sample is recorded in Fig. 5f. As seen, the minor overpotential increase of 21 mV at 50 mA cm^{-2} for 45 h is basically negligible. In contrast, the overpotential of the commercial RuO$_2$ catalyst sample increased by 47 mV under the same testing conditions, which was attributed to the electrochemical dissolution of RuO$_2$ at high potentials (Fig. S20). As understood, the potential difference between ORR and OER ($\triangle E = E_{j=10 \text{ mA cm-2}} - E_{1/2}$) can be used to evaluate the bifunctional catalytic performance of the target electrocatalyst [46]. As shown in Fig. 5g, the ΔE value of the Cu$_{NCs}$/Fe$_3$N-NPCF catalyst (0.66 V) is

slightly lower than those of the commercial 20% Pt/C+RuO$_2$ ($\Delta E = 0.68$ V), Cu$_{NCs}$-NPCF ($\Delta E = 0.79$ V) and Fe$_3$N-NPCF ($\Delta E = 0.72$ V) catalyst samples (Fig. S21-22 and Table S5). More importantly, the Mott-Schottky Cu$_{NCs}$/Fe$_3$N-NPCF catalyst exhibits an excellent dual performance in comparing with the $E_{j=10 \text{ mA cm-2}}$, $E_{1/2}$ and ΔE values derived from other non-PGM electrocatalysts (Fig. 5h and Table S6).

To evaluate the practical values of the prepared Cu$_{NCs}$/Fe$_3$N-NPCF bifunctional oxygen electrode catalyst, a liquid rechargeable ZAB was assembled based on the schematic diagram shown in Fig. 6a. During the tests, the air cathode was fabricated by anchoring Cu$_{NCs}$/Fe$_3$N-NPCF catalyst on metallic nickel foam. The zinc foil was used as anode and the 6.0 M KOH+ 0.2 M Zn(Ac)$_2$ solution was used as electrolyte [1,7,47]. As shown in Fig. 6b and Fig. S23, the open-circuit voltage (OCV) of the Cu$_{NCs}$/Fe$_3$N-NPCF-based ZAB was observed to be 1.48 V, which is higher than that of the commercial 20% Pt/C+RuO$_2$-based ZAB (1.40 V),
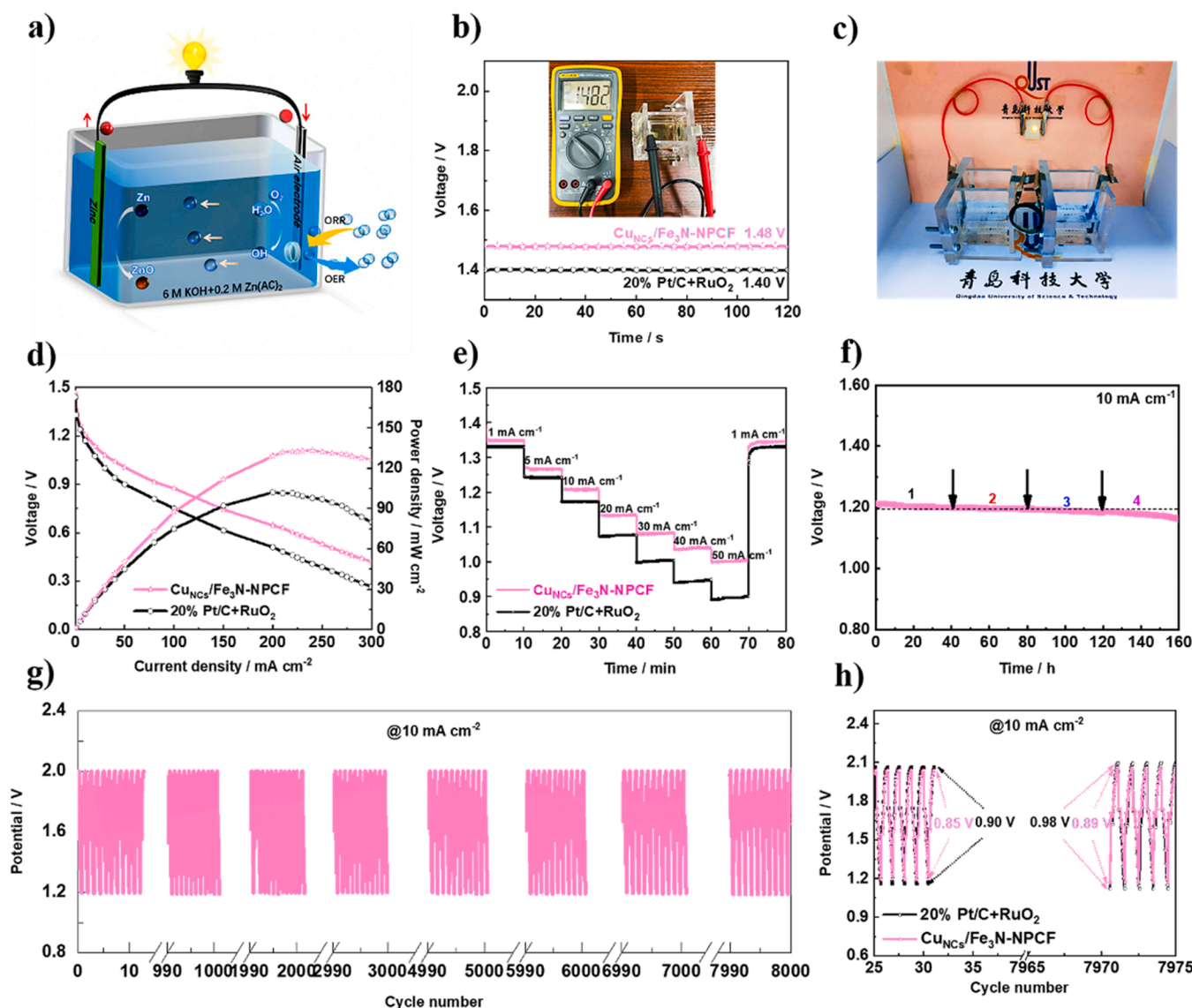
Fig. 6. (a) Schematic diagram of home-made ZABs. (b) Open circuit voltage (OCV) plots of the 20% Pt/C+RuO$_2$-based ZAB and the Cu$_{NCs}$/Fe$_3$N-NPCF-based ZAB (inset: OCV of the ZAB tested with a multimeter). (c) A photo of a light bulb illuminated by two assembled ZABs in series. (d) Discharge polarization (V-j) curves and the corresponding power densities, (e) Cell voltage vs. time at various current densities of the 20% Pt/C+RuO$_2$-based ZAB and the Cu$_{NCs}$/Fe$_3$N-NPCF-based ZAB. (f) Long-term galvanostatic discharge curve of the Cu$_{NCs}$/Fe$_3$N-NPCF-based ZAB that had been recharged by refilling with Zn foil four times. (g) Galvanostatic discharge-charge cycling profiles of the Cu$_{NCs}$/Fe$_3$N-NPCF-based ZAB at 20 mA cm^{-2}. (h) The corresponding voltage efficiency of the 20% Pt/C+RuO$_2$-based ZAB and the Cu$_{NCs}$/Fe$_3$N-NPCF-based ZAB during the discharge-charge cycling.

Cu$_{NCs}$-NPCF-based ZAB (1.34 V), and Fe$_3$N-NPCF-based ZAB (1.38 V), respectively. Fig. 6c illustrates that two Cu$_{NCs}$/Fe$_3$N-NPCF-based ZABs in series can power small light bulbs. The discharge polarization (V-j) curves in Fig. 6d show that the Cu$_{NCs}$/Fe$_3$N-NPCF-based ZAB achieves a maximum power density of 133.20 mW cm^{-2} at a current density of 235 mA cm^{-2}, which is much higher than those of the 20% Pt/C+RuO$_2$-based ZAB (101.50 mW cm^{-2}) and most of the reported non-PGM electrocatalysts-assembled ZABs (Table S7). Fig. 6e shows the discharge curves of the Cu$_{NCs}$/Fe$_3$N-NPCF-based ZAB at different current densities of 1–50 mA cm^{-2}. As observed, the Cu$_{NCs}$/Fe$_3$N-NPCF-based ZAB displays the stable discharge voltages of 1.21 V and 1.13 V when discharging at current densities of 10 and 20 mA cm^{-2}, respectively. While the discharge voltages of the commercial 20%Pt/C+RuO$_2$-based ZAB are 1.17 V and 1.07 V at current densities of 10 and 20 mA cm^{-2}, respectively. Besides, the Cu$_{NCs}$/Fe$_3$N-NPCF-based ZAB shows a smaller drop of discharge voltage compared to ZAB assembled from commercial 20%Pt/C+RuO$_2$ catalyst. More critically, the discharge voltage of the

Cu$_{NCs}$/Fe$_3$N-NPCF-based ZAB can restore to the initial value when the current density is switched back to 1 mA cm^{-2}, which implies an excellent rate capability. For comparison, the discharging profile of the Cu$_{NCs}$/Fe$_3$N-NPCF-based ZAB at a current density of 10 mA cm^{-2} is shown in Fig. 6f. Due to the dissolution and dendrites at the anode zinc foil in the discharging process, the discharge voltage dropped sharply after the continuous discharging for 40 h (Fig. S24). After constantly changing the zinc foil, the Cu$_{NCs}$/Fe$_3$N-NPCF-based ZAB show an excellent discharge stability by maintaining a stable discharge voltage at 10 mA cm^{-2} for 160 h [48]. Similarly, the Cu$_{NCs}$/Fe$_3$N-NPCF-based ZAB were also tested for 8000 charge-discharge cycles at a current density of 10 mA cm^{-2} to predict the practicality of the prepared Cu$_{NCs}$/- Fe$_3$N-NPCF catalyst. As observed in Fig. 6g, the assembled ZAB from Cu$_{NCs}$/Fe$_3$N-NPCF catalyst shows an initial voltage gap of 0.85 V at the first 30 charge-discharge cycles, which increases to 0.89 V at the end of the first 30 cycles. Compared to the voltage decay of the commercial 20%Pt/C+RuO$_2$-based ZAB with an initial voltage gap of 0.90 V and an

ending voltage gap of 0.98 V, the Cu$_{NCs}$/Fe$_3$N-NPCF-based ZAB displayed an excellent stability for practical rechargeable ZABs with a negligible voltage gap drop after 8000 charge/discharge cycles (Fig. 6h).

3.3. Analysis of the origin of catalytic activity

The electronic structures and valence states of the catalyst surfaces were investigated to reveal the ORR and OER reaction mechanisms of the prepared Cu$_{NCs}$/Fe$_3$N-NPCF heterocatalyst in alkaline electrolyte. According to the band theory of solids, electron transfer behavior is closely related to the Fermi level and work function of metals. The individual ionization energy value between metallic Cu$_{NCs}$-NPCF and Fe$_3$N-NPCF was compared by ultraviolet photoelectron spectroscopy (UPS) and this value was equivalent to the work function (Φ) of metallic material [49]. As shown in Fig. 7a, the work functions of Cu$_{NCs}$-NPCF and Fe$_3$N-NPCF are 6.61 eV and 7.56 eV, respectively. The differentiated UPS values of the Fermi levels from the Cu$_{NCs}$-NPCF and Fe$_3$N-NPCF samples provides the necessary conditions for the formation of the Mott-Schottky barrier and the potential for electron transfer. For the better demonstration, a Mott-Schottky structural model was established at the Cu/Fe$_3$N interface to probe the presence of Mott-Schottky barrier and electron transfer path within Cu$_{NCs}$/Fe$_3$N-NPCF catalyst structure. As shown in Fig. 7b, the differentiated work functions of the Cu and the Fe$_3$N two phases meets the requirements for building a Schottky barrier [50]. When the Mott-Schottky interface is formed between the Cu and Fe$_3$N two phases based on the Mott-Schottky effect, both the conduction band and the valence band of the Fe$_3$N phase will bend downward, and electrons can spontaneously transfer from the Cu phase to the Fe$_3$N

phase through the heterointerface until the Fermi levels on both sides are equal and an equilibrium state is established (Fig. 7c). Therefore, electrons will be enriched on the Fe$_3$N phase side to form the nucleophilic Fe$_3$N surface, while holes will accumulate on the Cu side to form the electrophilic Cu surface in the space charge region (Fig. 7d) [51]. In addition, the electronic effects in the Cu$_{NCs}$/Fe$_3$N-NPCF catalyst were further probed by X-ray photoelectron spectroscopy (XPS). More specifically, the high-resolution XPS Cu 2p and Fe 2p spectra of the Cu$_{NCs}$-NPCF, Fe$_3$N-NPCF and Cu$_{NCs}$/Fe$_3$N-NPCF catalyst samples are compared to explore the electronic interaction between Cu phase and Fe$_3$N phase. The high-resolution XPS Cu 2p peaks in Fig. 7e can be fitted into two main peaks of Cu 2p$_{3/2}$ and Cu 2p$_{1/2}$, as well as the two satellite peaks at 942.36 eV and 945.11 eV. Meanwhile, Cu 2p$_{3/2}$ peak can be split into Cu^0 (932.12 eV) and Cu (II) (934.87 eV), while Cu 2p$_{1/2}$ peak can be split into Cu^0 (952.32 eV) and Cu (II) (955.07 eV), respectively [6,39]. Due to the Fermi level asymmetry between the Cu and Fe$_3$N two phases, electrons will spontaneously transfer from the Cu phase to the Fe$_3$N phase. Compared with the Cu$_{NCs}$-NPCF sample, the high-resolution XPS Cu 2p peak of Cu$_{NCs}$/Fe$_3$N-NPCF sample shifted by 0.32 eV toward the higher binding energies, which implies the increased electron cloud density of Cu 2p orbitals. Similarly, the high-resolution XPS Fe 2p spectra of Fe$_3$N-NPCF and Cu$_{NCs}$/Fe$_3$N-NPCF two samples can be fitted into three peaks. They are assigned to Fe(II) (710.20 eV) and Fe(III) (713.58 eV) in the 2p$_{3/2}$ state, as well as the Fe(II) (723.20 eV) and Fe (III) (726.60 eV) and satellite peaks (717.70 eV) in the 2p$_{1/2}$ state, respectively [30,38]. Compared with Fe$_3$N-NPCF sample, the high-resolution XPS Fe 2p spectrum of Cu$_{NCs}$/Fe$_3$N-NPCF sample shifted by 0.40 eV toward the lower binding energies [52], and this indicates a
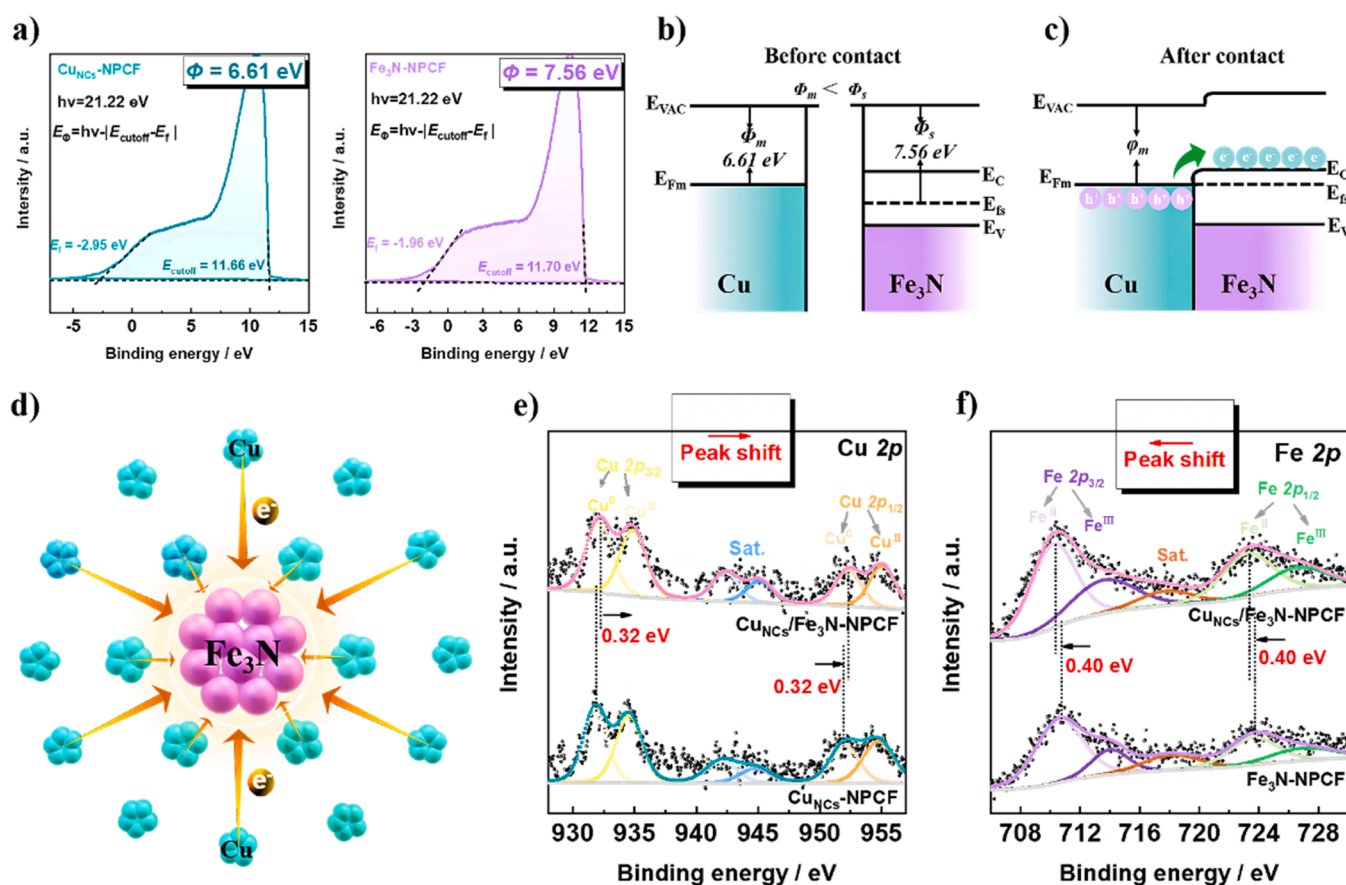

Fig. 7. (a) Ultraviolet photoelectron spectroscopy (UPS) spectra of Cu$_{NCs}$-NPCF and Fe$_3$N-NPCF samples. Energy band diagrams for Cu phase and Fe$_3$N phase: (b) before and (c) after contact, where E_{VAC} is vacuum energy, φ is vacuum electrostatic potential, E_F is Fermi level, E_C is conduction band, and E_V is valence band. (d) The schematic diagram of the charge transfer between Cu and Fe$_3$N phases. (e) Cu 2p XPS spectra of Cu$_{NCs}$-NPCF and Cu$_{NCs}$/Fe$_3$N-NPCF samples. (f) Fe 2p XPS spectra of Fe$_3$N-NPCF and Cu$_{NCs}$/Fe$_3$N-NPCF samples.

decrease in electron cloud density of Fe *2p* orbitals (Fig. 7f). Thus, the increase of Cu *2p* electron cloud density and the decrease of Fe *2p* electron cloud density enabled the spontaneous electron transfer between Cu phase and Fe$_3$N phase within Cu$_{NCs}$/Fe$_3$N-NPCF heterocatalyst structure based on Mott-Schottky effect, in which the Cu phase acts as the electron donor and the Fe$_2$O$_3$ phase acts as the electron acceptor [41, 53]. Compared with NPCF sample, the high-resolution XPS C *1 s* peak within Cu$_{NCs}$/Fe$_3$N-NPCF sample displays a slight negative shift in Fig. S25, which implies that a spontaneous transfer of electrons from Cu/Fe$_3$N metal ensembles to the carbon phase also occurred within the Cu$_{NCs}$/Fe$_3$N-NPCF composite (Fig. S26) [41]. In addition, since the increase of nitrogen content can enlarge the band gap of N-doped carbon and the work function of N-doped carbon is higher than that of the metal phase, more electrons can be extracted from the metal phase (Cu and Fe$_3$N) to N-doped carbon surfaces at the metal-carbon interface [54]. Under such metal-carbon substrate interactions, pyridine N is more receptive to form the metal-N$_x$ active sites with the adjacent electrons transferred from the metal phase and then passed through nitrogen atoms. The conjugation delocalization between the lone electron pair and the sp^2-hybridized carbon skeleton is transferred to the entire carbon body [55], so as that the catalytic activity can be further enhanced (Fig. S27).

By now, Tafel slopes in electrochemical studies, charge transfer resistance values in impedance spectra, H$_2$O$_2$ yields and electron transfer numbers during ORR process all indicated that the Mott-Schottky effect-driven spontaneous electron transfer within Cu$_{NCs}$/Fe$_3$N-NPCF heterocatalysts accelerated the electron transfer during the ORR/OER reaction and improved the catalytic activity. More likely, the difference in Fermi energy levels prompted strong electronic interaction between the Cu and Fe$_3$N phases. As a result, the electrons spontaneously transferred from the Cu phase to the Fe$_3$N phase via the carbon carrier. After electron rearrangement, the electrophilic region on Cu side improved the adsorption of oxygen molecules, increased the number of active sites, and thereby enhanced the electrocatalytic activity of oxygen reduction. While the nucleophilic region on the Fe$_3$N side further improved the adsorption of hydroxyl radicals, which resulted in a fast oxygen evolution reaction kinetics and exhibited more excellent electrocatalytic activity for oxygen evolution [32,56] (Fig. 8). Thus, the Cu$_{NCs}$/Fe$_3$N-NPCF Mott-Schottky catalyst exhibited the excellent bifunctional ORR and OER catalytic activities because of the structural advantages and strong electronic interaction.

4. Conclusion

In summary, the strategy of coupling metallic Cu/Fe$_3$N ensembles with different sizes with three-dimensional N-doped porous carbon nanosheets was demonstrated in preparing the Mott-Schottky Cu$_{NCs}$/Fe$_3$N-NPCF catalyst. The spontaneous electron transfer was achieved for efficient bifunctional oxygen electrocatalysis. The Mott-Schottky effect between Cu clusters and Fe$_3$N nanoparticles accelerated the electron supply from the active sites to various oxygen intermediates. The strong electronic interaction between electron-donor Cu and electron-acceptor Fe$_3$N phases improved the adsorption of O$_2$ and OH$^-$. As a result, the zinc-air battery assembled with Cu$_{NCs}$/Fe$_3$N-NPCF catalyst as the air cathode exhibited an excellent catalytic activity and durability with the peak power density up to 133.20 mW cm^{-2}. This strategy provides a new route in developing efficient and durable non-precious metal bifunctional oxygen electrocatalysts for the wide application of rechargeable ZABs.

CRediT authorship contribution statement

Qing Dong: Conceptualization, Investigation, Methodology, Formal analysis, Data curation, Visualization, Validation, Writing – review & editing. **Gangjian Li**: Data curation, Software, Visualization. **Fangfang Liu**: Methodology, Investigation, Data curation. **Jianwei Ren**: Formal
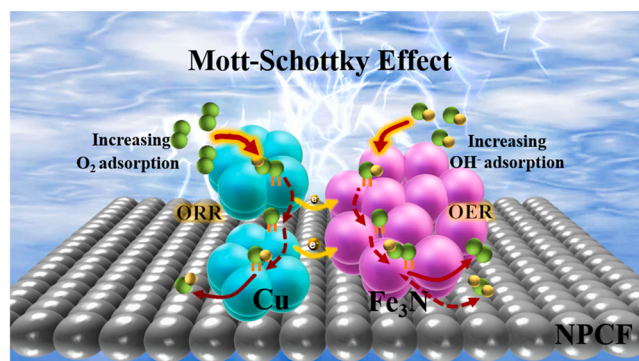

Fig. 8. The schematic ORR and OER catalytic mechanism of the Mott-Schottky Cu$_{NCs}$/Fe$_3$N-NPCF catalyst.

analysis, Investigation , Writing – review & editing. **Hui Wang**: Conceptualization, Supervision, Writing – review & editing. **Rongfang Wang**: Supervision, Project administration, Funding acquisition.

Declaration of Competing Interest

The authors declare that they have no known competing financial interests or personal relationships that could have appeared to influence the work reported in this paper.

Data Availability

No data was used for the research described in the article.

Acknowledgment

Appendix A. Supporting information

Supplementary data associated with this article can be found in the online version at doi:10.1016/j.apcatb.2023.122415.

References

[1] C.C. Weng, J.T. Ren, H.Y. Wang, X.W. Lv, Y.J. Song, Y.S. Wang, L. Chen, W. W. Tian, Z.Y. Yuan, Triple-phase oxygen electrocatalysis of hollow spherical structures for rechargeable Zn-Air batteries, Appl. Catal. B-Environ. 307 (2022) 121190–121200, https://doi.org/10.1016/j.apcatb.2022.121190.

[2] W.W. Tian, J.T. Ren, Z.Y. Yuan, In-situ cobalt-nickel alloy catalyzed nitrogen-doped carbon nanotube arrays as superior freestanding air electrodes for flexible zinc-air and aluminum-air batteries, Appl. Catal. B-Environ. 317 (2022) 121764–121776, https://doi.org/10.1016/j.apcatb.2022.121764.

[3] S. Siahrostami, Rechargeable metal-hydrogen peroxide battery, a solution to improve the metal-air battery performance, ACS Energy Lett. 7 (2022) 2717–2724, https://doi.org/10.1021/acsenergylett.2c01417.

[4] Y. Wang, J. Liu, T. Lu, R. He, N. Xu, J. Qiao, Ultra-high voltage efficiency rechargeable zinc-air battery based on high-performance structurally regulated metal-rich nickel phosphides and carbon hybrids bifunctional electrocatalysts, Appl. Catal. B-Environ. 321 (2023) 122041–122049, https://doi.org/10.1016/j. apcatb.2022.122041.

[5] J. Li, Y. Kang, Z. Lei, P. Liu, Well-controlled 3D flower-like CoP$_3$/CeO$_2$/C heterostructures as bifunctional oxygen electrocatalysts for rechargeable Zn-air batteries, Appl. Catal. B-Environ. 321 (2023) 122029–122041, https://doi.org/ 10.1016/j.apcatb.2022.122029.

[6] Q. Dong, H. Wang, J. Ren, X. Wang, R. Wang, Activating Cu/Fe$_2$O$_3$ nanoislands rooted on N-rich porous carbon nanosheets via the Mott-Schottky effect for rechargeable Zn-air battery, Chem. Eng. J. 442 (2022) 136128–136136, https:// doi.org/10.1016/j.cej.2022.136128.

[7] M. Wang, Z. Cao, L. Li, S. Ren, Porous Fe, N co-doped carbon with high electrocatalytic oxygen reduction performance in Zn-air battery, Carbon 200 (2022) 337–346, https://doi.org/10.1016/j.carbon.2022.08.068.

[8] A. Radwan, H. Jin, B. Liu, Z. Chen, Q. Wu, X. Zhao, D. He, S. Mu, 3D-ZIF scaffold derived carbon encapsulated iron nitride as a synergistic catalyst for ORR and zinc-air battery cathodes, Carbon 171 (2021) 368–375, https://doi.org/10.1016/j.carbon.2020.09.024.

[9] T. Li, Y. Hu, K. Liu, J. Yin, Y. Li, G. Fu, Y. Zhang, Y. Tang, Hollow yolk-shell nanoboxes assembled by Fe-doped Mn₃O₄ nanosheets for high-efficiency electrocatalytic oxygen reduction in Zn-air battery, Chem. Eng. J. 427 (2022) 131992–132001, https://doi.org/10.1016/j.cej.2021.131992.

[10] S. Li, B. Chen, Y. Wang, M.Y. Ye, P.A. van Aken, C. Cheng, A. Thomas, Oxygen-evolving catalytic atoms on metal carbides, Nat. Mater. 20 (2021) 1240–1247, https://doi.org/10.1038/s41563-021-01006-2.

[11] Y. Wang, Y. Jiang, Y. Zhao, X. Ge, Q. Lu, T. Zhang, D. Xie, M. Li, Y. Bu, Design strategies of perovskite nanofibers electrocatalysts for water splitting: A mini review, Chem. Eng. J. 451 (2023) 138710–138723, https://doi.org/10.1016/j.cej.2022.138710.

[12] H. Daimon, S.I. Yamazaki, M. Asahi, T. Ioroi, M. Inaba, A strategy for drastic improvement in the durability of Pt/C and PtCo/C alloy catalysts for the oxygen reduction reaction by melamine surface modification, ACS Catal. 12 (2022) 8976–8985, https://doi.org/10.1021/acscatal.2c01942.

[13] L. Zhang, H. Jiang, H. Liu, M.G. Kim, D. Yang, S. Liu, J. Cho, Sodium-decorated amorphous/crystalline RuO₂ with rich oxygen vacancies: a robust pH-universal oxygen evolution electrocatalyst, Angew. Chem. Int. Ed. 60 (2021) 18821–18829, https://doi.org/10.1002/anie.202106631.

[14] G.W. Sievers, A.W. Jensen, J. Quinson, A. Zana, F. Bizzotto, M. Oezaslan, A. Dworzak, J. Kirkensgaard, T. Smitshuysen, S. Kadkhodazadeh, M. Juelsholt, K. Jensen, K. Anklam, H. Wan, J. Schafer, K. Cepe, M. Escudero-Escribano, J. Rossmeisl, A. Quade, V. Bruser, M. Arenz, Self-supported Pt-CoO networks combining high specific activity with high surface area for oxygen reduction, Nat. Mater. 20 (2021) 208–213, https://doi.org/10.1038/s41563-020-0775-8.

[15] F. Ando, T. Gunji, T. Tanabe, I. Fukano, H.D. Abruña, J. Wu, T. Ohsaka, F. Matsumoto, Enhancement of the oxygen reduction reaction activity of Pt by tuning its d-band center via transition metal oxide support interactions, ACS Catal. 11 (2021) 9317–9332, https://doi.org/10.1021/acscatal.1c01868.

[16] X. Zhang, Y. Li, M. Jiang, J. Wei, X. Ding, C. Zhu, H. He, H. Lai, J. Shi, Engineering the coordination environment in atomic Fe/Ni dual-sites for efficient oxygen electrocatalysis in Zn-air and Mg-air batteries, Chem. Eng. J. 426 (2021) 130758–130768, https://doi.org/10.1016/j.cej.2021.130758.

[17] Y. Wang, N. Xu, R. He, L. Peng, D. Cai, J. Qiao, Large-scale defect-engineering tailored tri-doped graphene as a metal-free bifunctional catalyst for superior electrocatalytic oxygen reaction in rechargeable Zn-air battery, Appl. Catal. B-Environ. 285 (2021) 119811–119820, https://doi.org/10.1016/j.apcatb.2020.119811.

[18] K. Song, Y. Feng, X. Zhou, T. Qin, X. Zou, Y. Qi, Z. Chen, J. Rao, Z. Wang, N. Yue, X. Ge, W. Zhang, W. Zheng, Exploiting the trade-offs of electron transfer in MOF-derived single Zn/Co atomic couples for performance-enhanced zinc-air battery, Appl. Catal. B-Environ. 316 (2022) 121591–121601, https://doi.org/10.1016/j.apcatb.2022.121591.

[19] Y. Feng, K. Song, W. Zhang, X. Zhou, S.J. Yoo, J.-G. Kim, S. Qiao, Y. Qi, X. Zou, Z. Chen, T. Qin, N. Yue, Z. Wang, D. Li, W. Zheng, Efficient ORR catalysts for zinc-air battery: Biomass-derived ultra-stable Co nanoparticles wrapped with graphitic layers via optimizing electron transfer, J. Energy Chem. 70 (2022) 211–218, https://doi.org/10.1016/j.jechem.2022.01.047.

[20] C. Zhao, J. Liu, J. Wang, C. Wang, X. Guo, X. Li, X. Chen, L. Song, B. Li, Q. Zhang, A clicking confinement strategy to fabricate transition metal single-atom sites for bifunctional oxygen electrocatalysis, Sci. Adv. 8 (2022) 5091–5101, https://doi.org/10.1126/sciadv.abn5091.

[21] W.Y. Noh, J. Mun, Y. Lee, E.M. Kim, Y.K. Kim, K.Y. Kim, H.Y. Jeong, J.H. Lee, H. K. Song, G. Lee, J.S. Lee, Molecularly engineered carbon platform to anchor edge-hosted single-atomic M-N/C (M = Fe, Co, Ni, Cu) electrocatalysts of outstanding durability, ACS Catal. 12 (2022) 7994–8006, https://doi.org/10.1021/acscatal.2c00697.

[22] G. Yang, J. Zhu, P. Yuan, Y. Hu, G. Qu, B.A. Lu, X. Xue, H. Yin, W. Cheng, J. Cheng, W. Xu, J. Li, J. Hu, S. Mu, J.N. Zhang, Regulating Fe-spin state by atomically dispersed Mn-N in Fe-N-C catalysts with high oxygen reduction activity, Nat. Commun. 12 (2021) 1734–1743, https://doi.org/10.1038/s41467-021-21919-5.

[23] M. Mazzucato, G. Daniel, A. Mehmood, T. Kosmala, G. Granozzi, A. Kucernak, C. Durante, Effects of the induced micro- and meso-porosity on the single site density and turn over frequency of Fe-N-C carbon electrodes for the oxygen reduction reaction, Appl. Catal. B-Environ. 291 (2021) 120068–120081, https://doi.org/10.1016/j.apcatb.2021.120068.

[24] Q. Dong, Z. Mo, H. Wang, S. Ji, X. Wang, V. Linkov, R. Wang, N-doped carbon networks containing inserted FeNₓ@NC nanospheroids and bridged by carbon nanotubes as enhanced catalysts for the oxygen reduction reaction, ACS Sustain. Chem. Eng. 8 (2020) 6979–6989, https://doi.org/10.1021/acssuschemeng.0c00132.

[25] T. Li, M. Li, M. Zhang, X. Li, K. Liu, M. Zhang, X. Liu, D. Sun, L. Xu, Y. Zhang, Y. Tang, Immobilization of Fe₃N nanoparticles within N-doped carbon nanosheet frameworks as a high-efficiency electrocatalyst for oxygen reduction reaction in Zn-air batteries, Carbon 153 (2019) 364–371, https://doi.org/10.1016/j.carbon.2019.07.044.

[26] Z. Liu, J. Yu, X. Li, L. Zhang, D. Luo, X. Liu, X. Liu, S. Liu, H. Feng, G. Wu, P. Guo, H. Li, Z. Wang, X.S. Zhao, Facile synthesis of N-doped carbon layer encapsulated Fe₂N as an efficient catalyst for oxygen reduction reaction, Carbon 127 (2018) 636–642, https://doi.org/10.1016/j.carbon.2017.11.051.

[27] G. Li, J. Yu, W. Yu, L. Yang, X. Zhang, X. Liu, H. Liu, W. Zhou, Phosphorus-doped iron nitride nanoparticles encapsulated by nitrogen-doped carbon nanosheets on iron foam in situ derived from saccharomycetes cerevisiae for electrocatalytic overall water splitting, Small 16 (2020) 2001980–2001990, https://doi.org/10.1002/smll.202001980.

[28] H. Huang, C. Yu, X. Han, S. Li, S. Cui, C. Zhao, H. Huang, J. Qiu, Interface engineering of Ni₃N@Fe₃N heterostructure supported on carbon fiber for enhanced water oxidation, Ind. Eng. Chem. Res. 56 (2017) 14245–14251, https://doi.org/10.1021/acs.iecr.7b03351.

[29] W. Wang, J. Wang, S. Zhang, X. Song, B. Ma, Engineering of surface metal–nitrogen moieties in Fe-V based hybrid electrocatalysts for enhanced water oxidation, J. Mater. Chem. A 10 (2022) 12334–12340, https://doi.org/10.1039/d2ta02244c.

[30] K.A. Jannath, Y. Huang, K.D. Seo, D.S. Park, Y.B. Shim, Fe₃N decorated S/N doped carbon derived from a coordinated polymer as a bifunctional electrocatalyst for oxygen reduction and catecholamines oxidation, Carbon 187 (2022) 1–12, https://doi.org/10.1016/j.carbon.2021.10.074.

[31] L. Liu, A. Corma, Metal catalysts for heterogeneous catalysis: from single atoms to nanoclusters and nanoparticles, Chem. Rev. 118 (2018) 4981–5079, https://doi.org/10.1021/acs.chemrev.7b00776.

[32] Q. Zhang, F. Luo, X. Long, X. Yu, K. Qu, Z. Yang, N, P doped carbon nanotubes confined WN-Ni Mott-Schottky heterogeneous electrocatalyst for water splitting and rechargeable zinc-air batteries, Appl. Catal. B-Environ. 298 (2021) 120511–120519, https://doi./.1016/j.apcatb.2021.120511.

[33] H. Yang, B. Wang, S. Kou, G. Lu, Z. Liu, Mott-Schottky heterojunction of Co/Co₂P with built-in electric fields for bifunctional oxygen electrocatalysis and zinc-air battery, Chem. Eng. J. 425 (2021) 131589–131598, https://doi.org/10.1016/j.cej.2021.131589.

[34] C.H. Choi, M. Kim, H.C. Kwon, S.J. Cho, S. Yun, H.T. Kim, K.J. Mayrhofer, H. Kim, M. Choi, Tuning selectivity of electrochemical reactions by atomically dispersed platinum catalyst, Nat. Commun. 7 (2016) 10922–10930, https://doi.org/10.1038/ncomms10922.

[35] C. Dong, Y. Li, D. Cheng, M. Zhang, J. Liu, Y.G. Wang, D. Xiao, D. Ma, Supported metal clusters: fabrication and application in heterogeneous catalysis, ACS Catal. 10 (2020) 11011–11045, https://doi.org/10.1021/acscatal.0c02818.

[36] J. Zhang, Y. Deng, X. Cai, Y. Chen, M. Peng, Z. Jia, Z. Jiang, P. Ren, S. Yao, J. Xie, D. Xiao, X. Wen, N. Wang, H. Liu, D. Ma, Tin-assisted fully exposed platinum clusters stabilized on defect-rich graphene for dehydrogenation reaction, ACS Catal. 9 (2019) 5998–6005, https://doi.org/10.1021/acscatal.9b00601.

[37] Q. Dong, F. Zhang, S. Ji, X. Wang, H. Wang, V. Linkov, R. Wang, Fe₃C-inserted "tube plugging into porous network" nanohybrids as advanced sulfur hosts for lithium-sulfur batteries, J. Alloy. Compd. 877 (2021) 160286–160296, https://doi.org/10.1016/j.jallcom.2021.160286.

[38] M. Liang, M. Xie, E. Liu, C. Shi, C. He, N. Zhao, Ultrafine Fe₃N nanocrystals coupled with N doped 3D porous carbon networks induced atomically dispersed Fe for superior sodium ion storage, Carbon 196 (2022) 795–806, https://doi.org/10.1016/j.carbon.2022.05.052.

[39] J. Luo, Y. Cheng, H. Niu, T. Wang, C. Liang, Efficient Cu/FeOₓ catalyst with developed structure for catalytic transfer hydrogenation of furfural, J. Catal. 413 (2022) 575–587, https://doi.org/10.1016/j.jcat.2022.07.013.

[40] L. Han, K. Li, J. Sun, Q. Song, Y. Wang, Reinforcing effects of carbon nanotube on carbon/carbon composites before and after heat treatment, Mater. Sci. Eng. A 735 (2018) 10–18, https://doi.org/10.1016/j.msea.2018.08.025.

[41] Z. Sun, Y. Wang, L. Zhang, H. Wu, Y. Jin, Y. Li, Y. Shi, T. Zhu, H. Mao, J. Liu, C. Xiao, S. Ding, Simultaneously realizing rapid electron transfer and mass transport in jellyfish-like Mott-Schottky nanoreactors for oxygen reduction reaction, Adv. Funct. Mater. 30 (2020) 1910482–1910493, https://doi.org/10.1002/adfm.201910482.

[42] T. Tang, W. Jiang, X. Liu, J. Deng, S. Niu, B. Wang, S. Jin, Q. Zhang, L. Gu, J. Hu, L. Wan, Metastable rock salt oxide-mediated synthesis of high-density dual-protected M@NC for long-life rechargeable zinc-air batteries with record power density, J. Am. Chem. Soc. 142 (2020) 7116–7127, https://doi.org/10.1021/jacs.0c01349.

[43] Y. Wang, Q. Liu, X. Ge, F. Li, L. Chen, Z. Zhang, Z. Fu, Y. Lu, Y. Song, Y. Bu, Molecular-level proton acceptor boosts oxygen evolution catalysis to enable efficient industrial-scale water splitting, Green. Energy Environ. (2022), https://doi.org/10.1016/j.gee.2022.07.001.

[44] Y. Wu, H. Wang, S. Ji, B.G. Pollet, X. Wang, R. Wang, Engineered porous Ni₂P-nanoparticle/Ni₂P-nanosheet arrays via the Kirkendall effect and Ostwald ripening towards efficient overall water splitting, Nano Res. 13 (2020) 2098–2105, https://doi.org/10.1007/s12274-020-2816-7.

[45] Y. Niu, X. Teng, S. Gong, Z. Chen, A bimetallic alloy anchored on biomass-derived porous N-doped carbon fibers as a self-supporting bifunctional oxygen electrocatalyst for flexible Zn-air batteries, J. Mater. Chem. A 8 (2020) 13725–13734, https://doi.org/10.1039/d0ta03288c.

[46] P. Li, H. Wang, X. Tan, W. Hu, M. Huang, J. Shi, J. Chen, S. Liu, Z. Shi, Z. Li, Bifunctional electrocatalyst with CoN₃ active sties dispersed on N-doped graphitic carbon nanosheets for ultrastable Zn-air batteries, Appl. Catal. B-Environ. 316 (2022) 121674–121687, https://doi.org/10.1016/j.apcatb.2022.121674.

[47] Y. He, W. Shang, M. Ni, Y. Huang, H. Zhao, P. Tan, In-situ observation of the gas evolution process on the air electrode of Zn-air batteries during charging, Chem. Eng. J. 427 (2022) 130862–130870, https://doi.org/10.1016/j.cej.2021.130862.

[48] L. Song, T. Zheng, L. Zheng, B. Lu, H. Chen, Q. He, W. Zheng, Y. Hou, J. Lian, Y. Wu, J. Chen, Z. Ye, J. Lu, Cobalt-doped basic iron phosphate as bifunctional electrocatalyst for long-life and high-power-density rechargeable zinc-air batteries,

Appl. Catal. B-Environ. 300 (2022) 120712–120721, https://doi.org/10.1016/j.apcatb.2021.120712.

[49] Z. Li, Z. Gao, B. Li, L. Zhang, R. Fu, Y. Li, X. Mu, L. Li, Fe-Pt nanoclusters modified Mott-Schottky photocatalysts for enhanced ammonia synthesis at ambient conditions, Appl. Catal. B-Environ. 262 (2020) 118276–118282, https://doi.org/10.1016/j.apcatb.2019.118276.

[50] K. Gelderman, L. Lee, S.W. Donne, Flat-band potential of a semiconductor: using the Mott-Schottky equation, J. Chem. Educ. 84 (2007) 685–688, https://doi.org/10.1021/ed084p685.

[51] C. Li, Y. Liu, Z. Zhuo, H. Ju, D. Li, Y. Guo, X. Wu, H. Li, T. Zhai, Local charge distribution engineered by Schottky heterojunctions toward urea electrolysis, Adv. Energy Mater. 8 (2018) 1801775–1801782, https://doi.org/10.1002/aenm.201801775.

[52] K. Wang, W. Gao, P. Jiang, K. Lan, M. Yang, X. Huang, L. Ma, F. Niu, R. Li, Bi-functional catalyst of porous N-doped carbon with bimetallic FeCu for solvent-free resultant imines and hydrogenation of nitroarenes, Mol. Catal. 465 (2019) 43–53, https://doi.org/10.1016/j.mcat.2018.12.029.

[53] Z.H. Xue, J.T. Han, W.J. Feng, Q.Y. Yu, X.H. Li, M. Antonietti, J.S. Chen, Tuning the adsorption energy of methanol molecules along Ni-N-doped carbon phase boundaries by the Mott-Schottky effect for gas-phase methanol dehydrogenation, Angew. Chem. Int. Ed. 57 (2018) 2697–2701, https://doi.org/10.1002/anie.201713429.

[54] D. Zhu, M. Chen, Y. Huang, R. Li, T. Huang, J. Cao, Z. Shen, S.C. Lee, Tuning the nitrogen contents in carbon matrix encapsulating Co nanoparticles for promoting formaldehyde removal through Mott-Schottky effect, Appl. Surf. Sci. 583 (2022) 152552–152561, https://doi.org/10.1016/j.apsusc.2022.152552.

[55] T. Chen, S. Guo, J. Yang, Y. Xu, J. Sun, D. Wei, Z. Chen, B. Zhao, W. Ding, Nitrogen-doped carbon activated in situ by embedded nickel through the Mott-Schottky effect for the oxygen reduction reaction, Chemphyschem 18 (2017) 3454–3461, https://doi.org/10.1002/cphc.201700834.

[56] J. Wang, Q. Wei, Q. Ma, Z. Guo, F. Qin, Z.R. Ismagilov, W. Shen, Constructing Co@N-doped graphene shell catalyst via Mott-Schottky effect for selective hydrogenation of 5-hydroxylmethylfurfural, Appl. Catal. B-Environ. 263 (2020) 118339–118349, https://doi.org/10.1016/j.apcatb.2019.118339.